13 Surface Physics

T. Greber, R. Holzner, E. Wetli, J. Kröger, P. Schwaller,
J. Wider, H. J. Neff, C. Cepek, W. Auwärter, F. Baumberger, S. Berner,
M. Hoesch, A. Schneider, W. Deichmann, J. Osterwalder

In the surface physics laboratory we study well-defined surfaces of solid materials as well as adsorbed atomic and molecular monolayers and ultrathin films, prepared under ultrahigh-vacuum (UHV) conditions. In order to obtain detailed information on the geometric arrangement of the atoms within the first few monolayers of the surface we apply predominantly electron-based techniques such as x-ray photoelectron diffraction (XPD), medium-energy electron diffraction (MEED), low-energy electron diffraction (LEED), and more recently also scanning-tunneling and atomic force microscopy (STM/AFM - see below). A time-resolved MEED experiment is being developed with a temporal resolution in the picosecond range. Based on a new experimental geometry for XPD, where photoelectron diffraction effects are measured near a node of the photoexcited electron wave, the concept of photoelectron holography is tested as to whether it could finally fulfill its promises as a direct structural technique on surfaces.

Angle-resolved UV photoelectron spectroscopy (ARUPS) gives us access to the electronic band structure of solids and surfaces. Specifically, our experimental setup permits to directly map sections through the Fermi surfaces of such systems, which represent the electronic degrees of freedom relevant for transport properties, magnetic interactions and phase transitions. We could also extend the measuring range of photoemission above the Fermi level to observe thermally excited electrons within the band structure. An important asset of all these experiments is that the same probe (photoemission) gives us structural, electronic and magnetic information, and we can therefore study the interplay between these different degrees of freedom on the same sample.

In a common project with H. Keller we were able to purchase a combined STM/AFM system (Park Scientific) with one measuring head in UHV complementing our electron-scattering based techniques and one head working at ambient pressure serving as a general purpose surface characterization tool for the Physics Department and other interested departments. The UHV head has been mounted on a dedicated UHV chamber which also contains a basic sample preparation facility, and which can eventually be connected to our photoelectron spectrometer. The high efficiency of the vibration isolation of the chamber and the STM head is demonstrated by atomic resolution images on metal surfaces (Ni(111), Au(111)) measured with a turbomolecular pump running. This instrument is now an important element in our pool of surface analytical tools (see section 13.2).

We have continued our collaboration with the surface chemistry group of Prof. J. R. Huber of the Physical Chemistry Department (P. Willmott, H. Manoravi, H. Spillmann, N. Baiker) who have developed excellent thin film preparation capabilities using pulsed reactive crossed-beam laser ablation. They have grown single crystalline films of several materials of high technological relevance (TiC_xN_{1-x}, GaN, Ti:Al_2O_3, SiN_x and CN_x), and they were using our photoelectron spectrometer for surface composition analysis and for verifying the crystallinity of their films.

In a new collaboration with Prof. M. Sancrotti (TASC Laboratory of the Istituto Nazionale per la Fisica della Materia, Trieste, Italy) we investigate structual and electronic properties of C_{60} monolayer films on metal surfaces.

13.1 X-ray photoelectron diffraction in the backscattering geometry

The precise knowledge of the adsorption geometry of atoms, molecules and molecular fragments on metal surfaces is one of the keys to understanding the mechanisms of catalytic activity and selectivity. XPD has not been a very fruitful technique for this type of problem, since the strong forward scattering signals of the photoelectrons excited from the adsorbates point into the crystal and therefore cannot be measured. In the course of our study of the oxygen-covered Rh(111) surface we could measure for the first time the weak backscattering signals in adsorbate emission, and we were able to show that these signals are uniquely sensitive to the oxygen bonding distance to the surface and to the bonding site [1]. Fig. 13.1

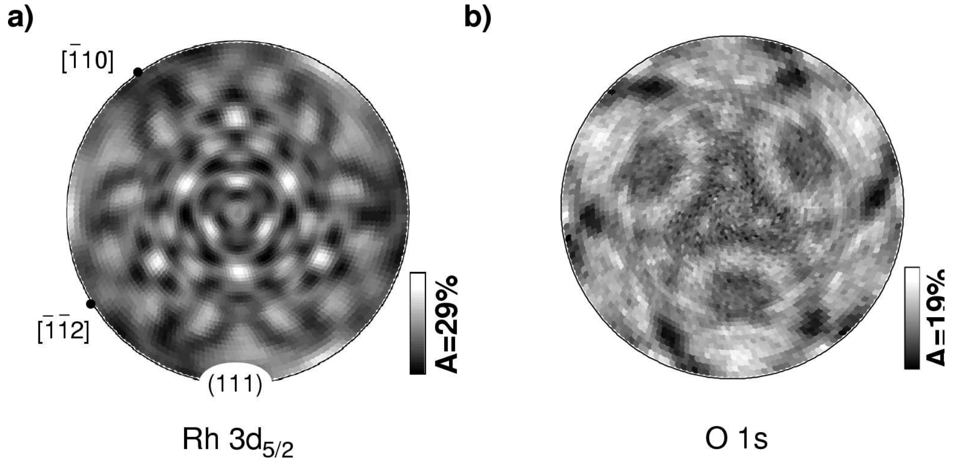

Figure 13.1: *Measured photoelectron diffraction patterns a) for Rh $3d_{5/2}$ emission (E_{kin}=947 eV) from a clean Rh(111) surface, and b) for O 1s emission (E_{kin}=723 eV) from a (2x1)-1O/Rh(111) surface. The data are stereographically projected. Intensities are represented in a linear grey scale with grey bars indicating the overall anisotropy $A = (I_{max} - I_{min})/I_{max}$ for each pattern.*

shows full XPD patterns of Rh $3d_{5/2}$ substrate emission and of O $1s$ adsorbate emission. The substrate pattern provides the structure and the orientation of the crystal lattice to which the adsorbate structure can be referenced. In the adsorbate pattern the most prominent features are three ring-like structures arranged in a threefold symmetric fashion. They represent circles of constructive interference of electrons emitted from the O atoms directly and electrons backscattered by nearest-neighbour Rh atoms. The centers of the circles are related with the oxygen to rhodium bond directions, while the circle radii are a measure for the bond distance. This is further illustrated in fig. 13.2, where we give single-scattering cluster calculations for O emission using oxygen near-neighbour configurations of different bond lengths and sites. The site is identified immediately by the orientation of the three-circle pattern, while the circles are seen to be very sensitive to changes of 0.1 Å in the adsorption height z_0. Given the accuracy with which we can measure these backscattering signals we estimate a precision in bond length of ±0.02 Å.

13.2 Hexagonal boron nitride films on Ni(111)

Metal-insulator-metal structures are very important as tunneling junctions between any combination of normal metals, ferromagnets or superconductors. The ultimate junction is reached with a single monolayer of insulating material. Recently it was discovered that very stable monolayers of hexagonal boron nitride (h-BN) can be prepared by the reaction of benzene-

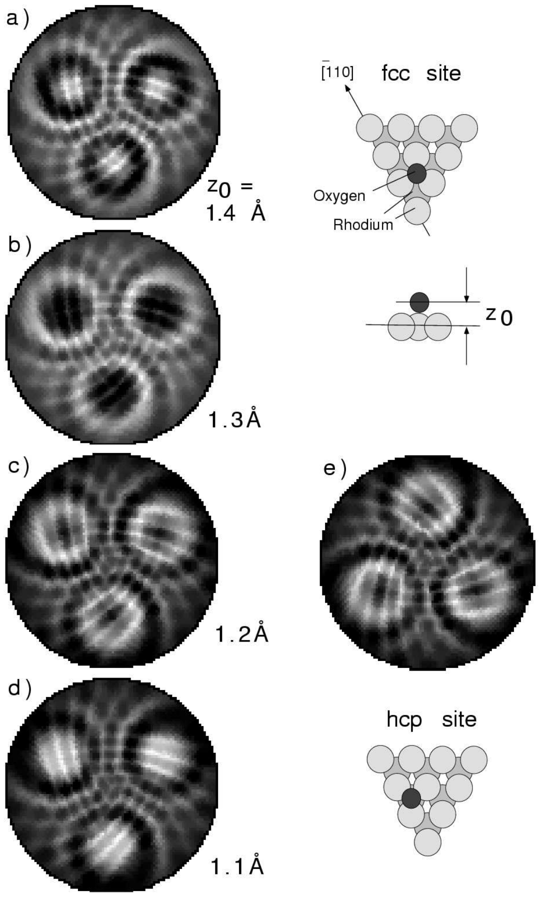

Figure 13.2: *XPD single scattering cluster calculations for O 1s emission at E_{kin}=723 eV for simple four-atom clusters representing one oxygen atom and three nearest-neighbour Rh atoms forming a threefold hollow adsorption site. In a)-d) the O atom occupies the fcc site at various bond distances (see illustration), while e) shows the adsorption in the hcp site.*

like borazine $(BN)_3H_6$ with Ni(111) at 1100K [2]. With the aim of studying the electronic and magnetic coupling across such films we characterized their growth by XPD and by STM. From the XPD analysis we learn that film growth stops before a second layer starts to form [3]: Strong forward scattering signals in both B 1*s* and N 1*s* emission would reveal second layer formation already at the percent level.

Fig. 13.3 shows two STM images of such monolayers recorded in our new UHV-STM chamber. The image (a) shows a wide area scan of 3000 x 3000 Å. The film is extremely flat, and the density of monoatomic steps is lower than it was on the Ni(111) substrate before growth, suggesting that the borazine exposure at high temperature induces long range mass transport of Ni atoms flattening the surface. No defects are observed at this scale. The image (b) shows a much smaller area with atomic resolution. A periodic hexagonal pattern with a lattice constant of 2.5 Å is found, consistent with epitaxial *h*-BN on Ni(111). At this point of our investigation it is not clear which states contribute to the tunneling signal in this image: At the low tunneling voltage (tungsten tip at +4.8 mV) one does not expect to reach electronic states of the boron nitride which has a band gap of 5.2 eV in its bulk form. We may observe tunneling of Ni electrons through this thin insulating barrier, or maybe

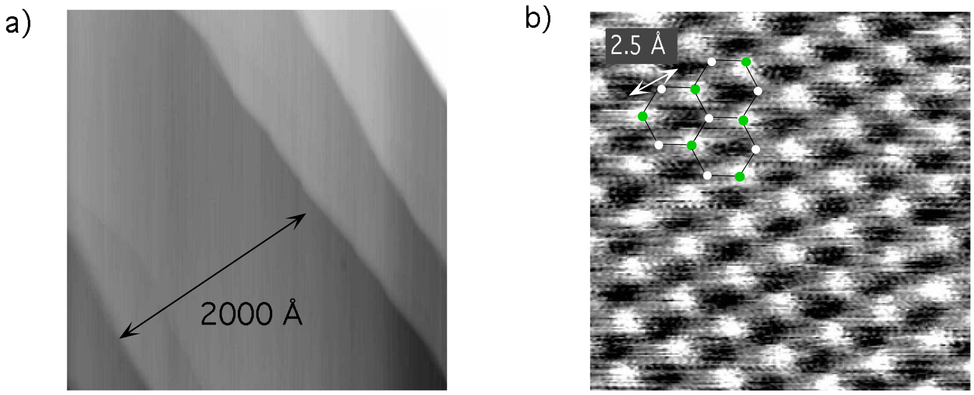

Figure 13.3: *STM images of h-BN on Ni(111): a) large area topography; b) atomic resolution image of h-BN. The overlayed drawing illustrates the structure of this film. We do not yet know which atom within the unit cell causes the bright spots, i.e. the structure model is arbitrarily placed within the image.*

the monolayer of h-BN on Ni(111) is no longer an insulator. This issue is currently under investigation.

We have thus confirmed that these films are not only flat and limited to one monolayer (XPD) but that they are highly contiguous and defect-free. They represent thus an ideal system for studying metal-insulator-metal structures at monolayer definition. Preliminary results show that cobalt can be grown on such films in a wide variety of morphologies, ranging from rather monodisperse small circular clusters to larger flat islands of regular triangular shape and to thick, contiguous films of rather high roughness.

13.3 Time-resolved medium-energy electron diffraction

We are developing an experimental method for obtaining structural information on solid surfaces on a very short time scale. For this purpose, we generate a pulsed electron beam of typically 2 keV energy and measure the angular distribution of the backscattered electrons on a channelplate detector: medium-energy electron diffraction (MEED). The electron pulses are produced by shining femtosecond laser pulses on a photocathode. Considering the electron optical properties of our electron gun we expect electron pulses of a few picoseconds duration [4]. The number of electrons in a single pulse is naturally not sufficient to create a measurable diffraction pattern on the screen, and thus we have to operate the experiment in a pump-probe mode where we periodically prepare the surface in a defined way at a certain time t_0 and have the electron pulse impinge on the surface with a defined delay dt. In order to achieve picosecond resolution in the delay, the preparation step must necessarily be triggered by a laser pulse which is temporally correlated with the probe electron pulse.

A Ti:sapphire laser system in our laboratory produces femtosecond pulses of nanojoule energies at a repetition rate of 80 MHz. This laser works at a wavelength of 800 nm. For the production of the electron pulses at the photocathode we have to double the optical frequency using a nonlinear crystal (BBO). A pulse compression line has been built for higher photoemission efficiency. Using a beam splitter and a computer-controlled optical delay line we have characterized the pulse width to be 90 fs by refocusing the delayed and undelayed beams onto the Ag photocathode. Ag serves as an autocorrelator because at the work function of 4.3 eV two photons of 3 eV are required for producing a photoelectron.

We have started an investigation of the system Pb/Ge(111). At 1/3 of a monolayer of Pb this system presents a $(\sqrt{3} \times \sqrt{3}) - R30°$ structure at room temperature. Below 280 K, this surface forms a charge density wave with a (3×3) symmetry [5]. Our aim is to study the dynamics of this charge density wave formation by time-resolved MEED (t-MEED). As a first step, we have to demonstrate that MEED is sufficiently surface sensitive so we can detect signals that are related to the 1/3 monolayer of Pb. With electron mean free paths of typically 20-40 Å at 2 keV this is by no means easy. In order to enhance the surface signal we have to go to a scattering geometry where the electrons hit the surface at a very shallow angle of less than 5° and measure the scattered electrons also along directions close to the surface. In fig. 13.4 we show a difference image of two MEED patterns, one taken with a 1/3

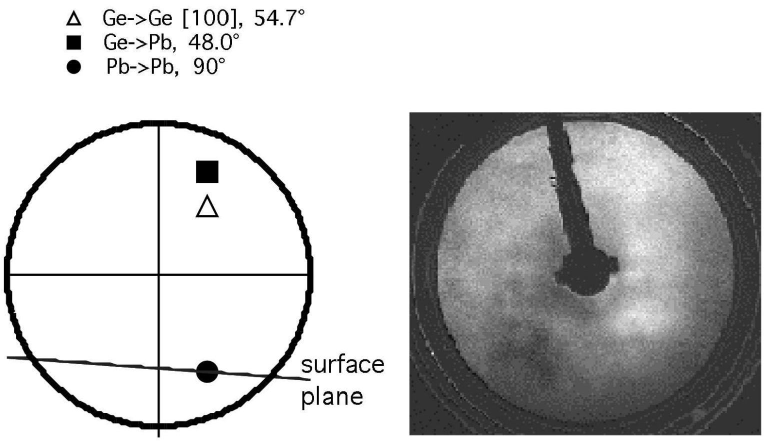

Figure 13.4: *Right: Difference image of two MEED patterns, one measured with 1/3 monolayer of Pb on Ge(111) and one measured on clean Ge(111). The shadow of the standard LEED electron gun is visible in the center of the plot. Left: Schematic drawing of relevant forward scattering directions as they should appear on the MEED screen. Note that the sample is strongly tilted about a horizontal axis such that the Ge(111) surface plane intersects the screen.*

monolayer of Pb on the Ge(111) surface, and one for the clean Ge(111) surface where the Pb has been removed by heating the crystal. The difference image shows enhanced intensity around positions where forward scattering off Pb atoms is expected to occur (see schematic drawing). While these Pb-related scattering signals are rather weak, it appears that they can be extracted from such difference plots.

13.4 Near-node photoelectron holography

If photoelectron diffraction is measured near a node of the photoelectron source wave the true diffraction intensity is enhanced and holographic interpretation of such data should become feasible [6]. The set up of the new photoelectron diffraction experiment that will meet the requirements for near-node photoelectron holography was further completed (see

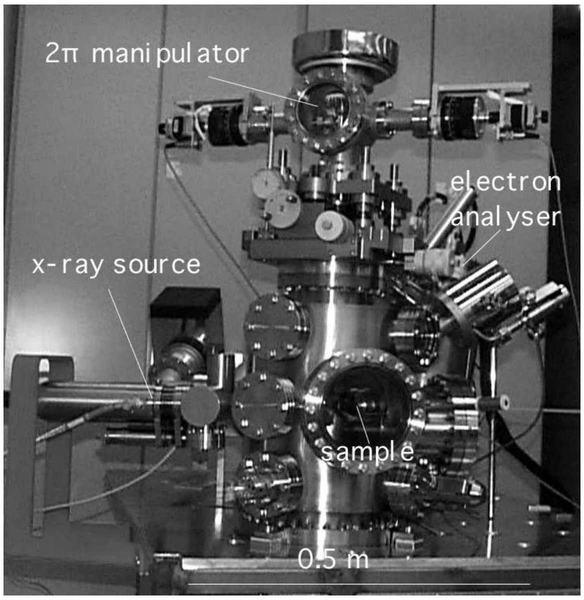

Figure 13.5: *Photograph of the near-node photoelectron diffraction experiment as installed in our laboratory.*

fig. 13.5). To date the chamber with the collimated (and monochromatized) Al $K\alpha$ x-ray source, the electron analyzer and the home built 2π manipulator that allows the detection of photoelectrons in all directions above the surface are implemented in the experiment. Particular attention has been payed to the cooling of the sample across a sliding contact in our manipulator. We currently reach temperatures below 60 K.

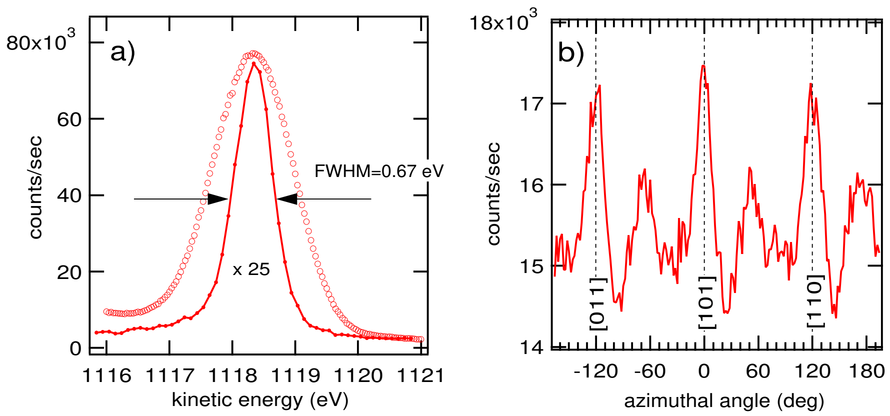

Figure 13.6: *First photoemission data from the new experimental setup, recorded from Ag(111). a) Normal emission x-ray photoemission spectrum (XPS) of the Ag* $3d_{5/2}$ *core level for high energy resolution (FWHM=500 meV, dots), and for high transmission (open circles) as used for diffraction experiments. The x-ray power is 600 W, the x-ray angle-of-incidence is* 45° *relative to the electron detector (standard geometry). b) Ag* $3d_{5/2}$ *photoemission intensity at* 35° *polar emission angle as a function of the azimuthal angle. The three prominent peaks correspond to the well-known forward scattering features along the* $<110>$ *atomic chains.*

In fig. 13.6 first experimental photoelectron data, still recorded in the standard geometry, are shown. Fig. 13.6a depicts an Ag $3d_{5/2}$ core level spectrum from an Ag(111) single crystal surface. In fig. 13.6b an azimuthal diffraction pattern of Ag $3d_{5/2}$ emission at a polar angle of 35° away from the surface normal is shown. The three $< 110 >$-type forward scattering peaks are clearly resolved. After implementation of an electron transfer lens, permitting to have the electron detection direction only 15° away from the x-ray incidence direction, the near-node experiment will be performed.

Recent experiments at the ALOISA beamline at the ELETTRA synchrotron in Trieste allowed us to test the theoretical predictions for the relative enhancement of higher-order diffraction compared to zero-order diffraction, that is forward scattering.

13.5 Photoemission from oriented orbitals

Ultraviolet-excited photoemission is widely used for studying energy levels of molecules and solids. The interpretation of spectra usually takes into account proper initial state wave functions, while little attention has been given to scattering effects in the photoemission final state. Recently, we discovered that, much like in XPD, the intensities of UV-excited spectral features in valence emission from Cu surfaces are dominated by scattering effects in the photoemission final state [7]. Moreover, the angular intensity pattern is found to be very sensitive to the angular momentum of the emitted electrons.

If final state scattering is present in such ultraviolet photoelectron diffraction (UPD) data, they should contain structural information. From their angular momentum sensitivity one can, thanks to the photoemission selection rules, identify the character of the wave functions. We have tested this idea by using a well-characterized molecular adsorbate system: carbon monoxide on Ni(111) [8]. In fig. 13.7 the spectra show Ni $3d$ emission between 38.0 and

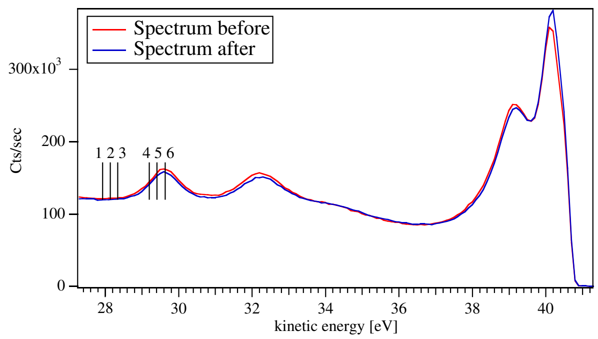

Figure 13.7: *UV photoelectron spectra excited with He IIα radiation before and after a one-hour UPD measurement. The positions of the six channeltron detectors used for the data of fig. 13.8 are indicated.*

40.8 eV, while the CO 4σ and 5σ molecular levels appear at kinetic energies of 29.7 and 32.4 eV, respectively. By setting the detectors according to the positions as indicated in the figure we have measured the angular modulation of 4σ emission. After subtracting the corresponding background (detectors 1-3) the patterns as shown in fig. 13.8 are generated for excitation by He IIα and He IIβ radiation.

We use the single scattering theory of XPD as a starting point for the description of these data. While XPD describes emission from core levels situated on a well defined atom, emission from a molecular state has to be viewed as a coherent emission process from two centers. In a linear combination of atomic orbitals (LCAO) picture, the amplitude and phase

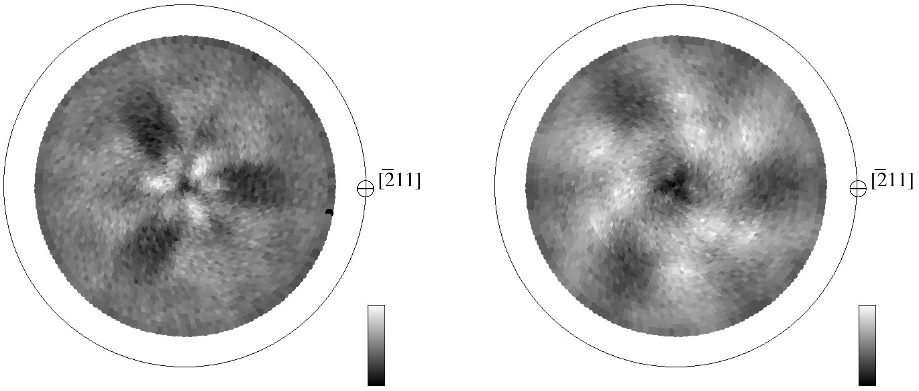

Figure 13.8: *Measured angular distributions of photoelectrons from CO 4σ orbitals on Ni(111) excited with He IIα (left) and He IIβ (right) radiation.*

of each atomic orbital on either the carbon or the oxygen atom needs to be known. The final state scattering of each atomic orbital can be calculated using the single scattering model. From the coherent superposition of all the emission and scattering amplitudes the intensities can be calculated. The results of these calculations for the present case are rather encouraging. For the particular system of CO/Ni(111) we obtain fairly good agreement with experiment for a structure where CO molecules sit upright (carbon down) and preferentially in threefold hollow adsorption sites.

13.6 Photoemission Fermi edge as a thermometer

The temperature of a sample in thermal equilibrium manifests itself in the width of the Fermi edge in photoemission spectra. However, in ARUPS the shape and even the position of the Fermi edge can be markedly changed by Fermi level crossings of bands. The spectrum shown in fig. 13.9b is taken from a clean Ni(111) surface along a direction where the two spin-split d bands (d↑ and d↓) straddle the Fermi energy [9]. The presence of the d↓) band slighly above E_F lifts the tail of the Fermi edge strongly and makes it look shifted to negative binding energies. From measurements of such spectra along many angles we can separate the contributions of the bands and of a featureless background, such as demonstrated in fig. 13.9a. If we now plot the intensity of the background as a function of energy, we recover nice Fermi-Dirac distribution functions centered at the true Fermi level (fig. 13.9b). From these functions, the sample temperature can be fitted to an accuracy of the order of 10 K. The benefit of this procedure is that we obtain a measure of the temperature of the surface under study even in the presence of spacial or temporal temperature gradients.

13.7 Underdoping of Bi-cuprates by ultraviolet radiation

in collaboration with P. Willmott, Physikalische Chemie, Universität Zürich

During our study of the Fermi surface of Bi-type high temperature superconductors at various doping levels we noted that the spectra of optimally doped $Bi_2Sr_2CaCu_2O_8$ (Bi2212) undergo marked changes when the sample is exposed to the intense ultraviolet ratiation of our He discharge lamp. We have characterized these changes very carefully and were able to show that they are associated with radiation-induced oxygen desorption [10]. From measurements of characteristic Fermi surface features it is found that the oxygen desorption causes a decrease

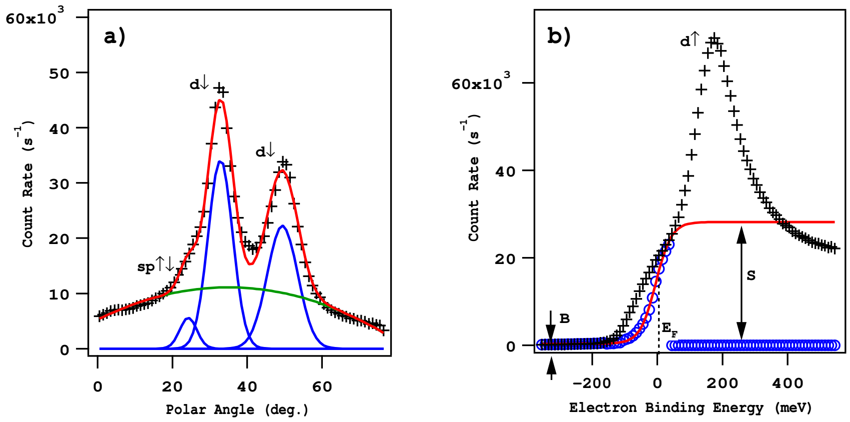

Figure 13.9: *a) He I excited photoemission intensity at the Fermi level from Ni(111) measured as a function of polar emission angle. The crosses show the measured intensities, while the solid lines indicate the Gaussians of the band crossings and the parabolic background function used to fit the measured data. b) (+) photoemission spectrum measured at a polar angle of* 40°. *(○) intensity of the fitted background (from a)) as a function of binding energy.*

of the doping level of the cuprate. The desorption cross sections are strongly dependent on the photon energy: 188 ± 53 kb for He II and 23 ± 6 kb for He I radiation (1 barn = $10^{-24}cm^2$). Two different oxygen desorption channels are inferred from this difference. With He II radiation ($h\nu$ = 40.8 eV) the O 2s level can be excited. During the following Auger decay a neutral oxygen species can form which may desorb very effectively, accounting for the strong increase in the desorption cross section.

Attempts to observe the radiation-induced underdoping of thin films of $YBa_2Cu_3O_{6+x}$ in resistivity measurements failed due to the roughness of the prepared films. For these experiments, a versatile UHV-based contact system for four-point resistivity measurements has been developed and successfully tested on a thick $YBa_2Cu_3O_{6+x}$ film.

13.8 Evolution of the Fermi surface in a transition metal film

in collaboration with P. Aebi, Institut de Physique, Université de Fribourg

Magnetic multilayers, i.e. structures of alternating layers of a ferromagnetic and a non-ferromagnetic material are of great technological interest for their strong magnetoresistance effects [11]. The magnetic coupling between the ferromagnetic layers is believed to be strongly influenced by the Fermi surface of the nonmagnetic material [12]. In these models, bulk Fermi surface data are usually the starting point for these considerations. However, since the layers can be only a few atomic layers thick, it is by no means clear whether this assumption is justified.

We studied the evolution of the Fermi surface with layer thickness for the ferromagnetic layer in a film of cobalt on Cu(111). This is one of the prototype magnetic multilayer systems. The growth has been characterized by several groups [13]. The formation of hexagonal close-packed (hcp) Co sets in after 1-3 monolayers (ML) of pseudomorphic growth by introducing more and more stacking faults on the face-centered cubic (fcc) structure of the substrate and the interface. In fig 13.10 a Fermi surface map of clean Cu(111) is shown, measured at a photon energy of 21.21 eV. A section through the bulk Fermi surface is seen, intersecting three of the necks of this textbook Fermi surface. In the center of the image, the well-known

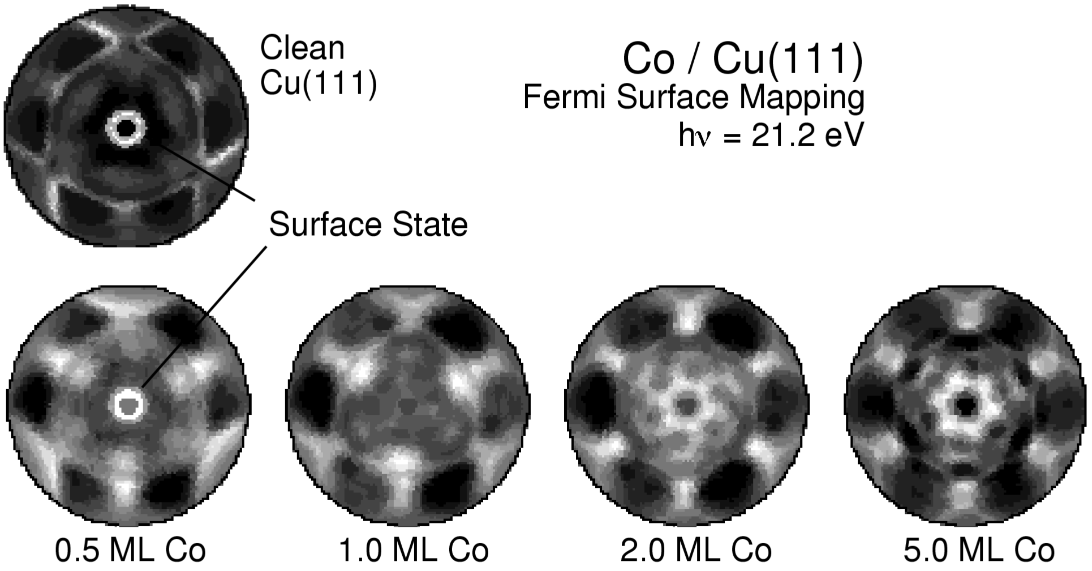

Figure 13.10: *Photoemission Fermi surface maps for clean Cu(111) and Co films of various thicknesses grown on Cu(111), excited with He Iα radiation.*

Shockley surface state appears (see next section). Onto this surface, Co films of thicknesses ranging from 0.5 to 5 monolayers have been deposited and characterized by XPD. The Fermi surface maps in fig. 13.10 show that the Cu Fermi surface contours get very diffuse at 0.5 ML, due to the strong scattering of the electrons in the disordered surface layer. The surface state gets completely suppressed at a coverage of 1 ML. At 2 ML, where XPD shows a substantial fraction of stacking faults, i.e. an hcp-like structure, the Fermi surface map approaches a sixfold symmetry. At 5 ML a rather sharp Fermi surface image results. Comparison of this map to Fermi-contours obtained from bandstructure calculations indicates that the Fermi surface has essentially converged to that of bulk cobalt as seen through the (0001) surface. We also measured the energy dispersion of the cobalt bands and find that the Co band structure forms very rapidly, essentially with the first monolayer.

13.9 Surface states on vicinal Cu(111) surfaces

In fig. 13.10 we have seen the Shockley surface state of the clean Cu(111) surface [14] to exhibit a circular Fermi surface centered around normal emission (center of the plot). This state is a consequence of the broken translational symmetry in the normal direction at the crystal surface, and it is located in the band gap of the surface-projected bulk bands. The wave functions propagate parallel to the surface and fall off exponentially both towards the vacuum and towards the bulk and are thus two-dimensional. The circular shape of the Fermi surface and the parabolic dispersion (not shown) indicates that these surface state electrons are free to a good approximation.

Atomic steps on an otherwise flat surface act as scattering centers for surface state electrons. Surfaces that are cut slightly off the Cu(111) planes (vicinal surfaces) exhibit more or less uniform terraces of (111) orientation separated by equidistant steps. We selected Cu(332) and Cu(221) surfaces with terrace geometries as depicted in fig. 13.11 in order to study the influence of the terrace width on the Fermi surface and on the dispersion of the surface state. Fig. 13.12 shows blow-ups of the Fermi surface maps as measured on the three different

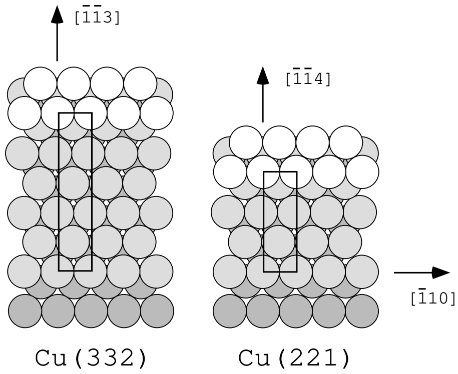

Figure 13.11: *Expected surface atomic configuration for an ideal Cu(332) and Cu(221) surface, respectively. Terrace widths L and miscut angles α are: 12 Å and $10°$ for Cu(332), and 7.7 Å and $15.8°$ for Cu(221). Primitive surface unit cells are indicated by rectangles. The indicated directions lie in the surface planes.*

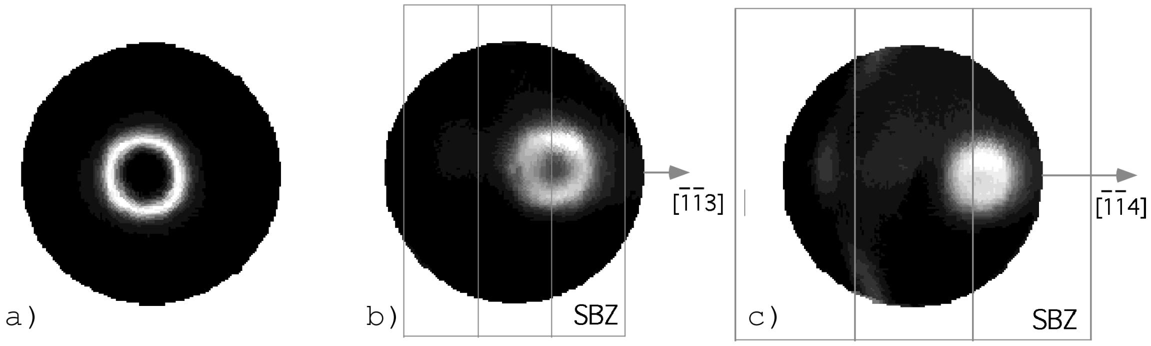

Figure 13.12: *High-resolution He I excited Fermi surface maps of a) Cu(111), b) Cu(332) and c) Cu(221). Surface Brillouin zones are indicated for the stepped samples. The centers of the plots represent emission along the macroscopic surface normal, while the given directions lie in the surface plane and point "up" the steps. The weak feature on the left side in the Cu(221) measurement is due to intersections with the bulk Fermi surface.*

surfaces. We see several things: From carefully fitting the data we find that the surface state Fermi surfaces remain circles for Cu(111) and Cu(221) while for Cu(332) there is a slight deviation. This indicates that the electrons remain nearly free and that no standing waves are formed. The dispersion remains parabolic with slight changes in the effective mass (not shown). The Fermi surfaces of the stepped surfaces move away from the surface normal and along the tilt direction of the local (111) facets. However, the angular displacement is less than the actual tilt; the Fermi surfaces appear to be tied to the boundaries of the surface Brillouin zones. With decreasing terrace length (higher miscut angle) the Fermi surfaces become smaller, i.e. the surface state gets depopulated. From fitting the areas of the Fermi surfaces we find that the population is reduced from 0.07 electrons per Cu surface atom on Cu(111) to 0.02 electrons on Cu(221). This behaviour is in qualitative agreement with a one-dimensional Kronig-Penney model where the steps are represented by a periodic sequence of delta functions. The depopulation is thus a consequence of the electron confinement on the short terraces. At the same time, the Fermi surface contours become broader, which is due to the increased coupling of the surface state wave functions to the bulk states.

13.10 Velocity-selective optical pumping due to back reflection of resonant laser light in a thin sodium vapor cell

On our way to demonstrate beamswitching [15, 16] in a thin sodium vapor cell (sandwich cell) we measured the absorption of laser light resonant to the atomic D_1 transition at 589 nm using the experimental setup shown in fig. 13.13. To our surprise we found the absorption

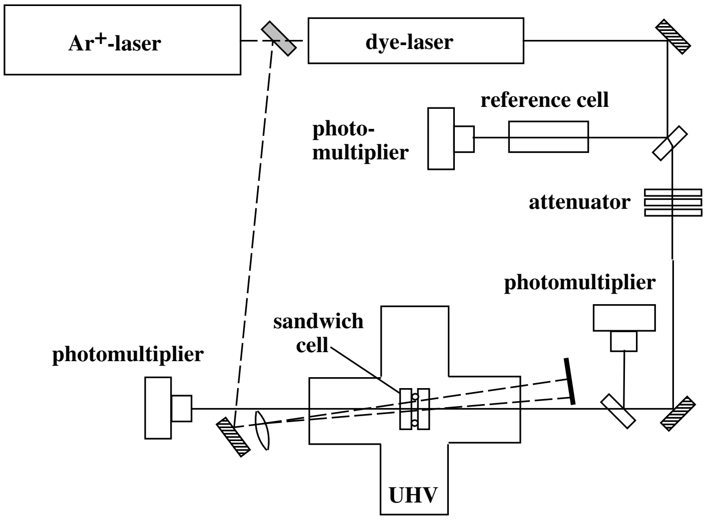

Figure 13.13: *Experimental setup: Beam from the Ar-ion laser (dashed line) evaporates Na in the sandwich cell; resonant beam from the dye laser (full line).*

profile (fig. 13.14) with a very narrow width at exact resonance and without the typical two-bump shape shown by the absorption profile of a reference vapor cell. The explanation for this

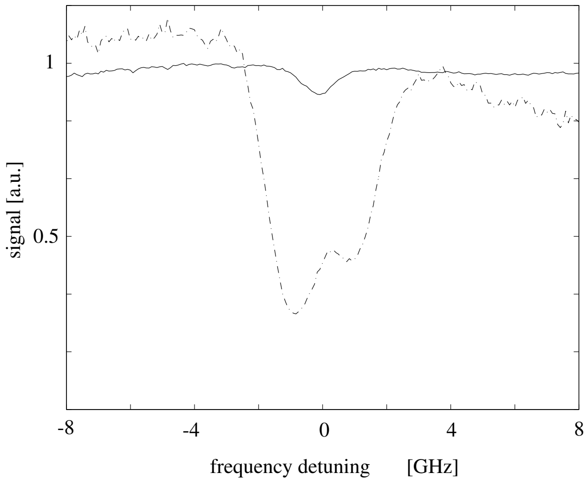

Figure 13.14: *Solid line: transmitted power through the sandwich cell near the D_1 resonance of Na; dash-dotted line: transmitted power through the reference cell.*

unexpected absorption profile is as follows: part of the transmitting beam is backreflected by the surface of the rear window of the thin cell. Therefore atoms with specific velocity components parallel to the direction of the laser beam and the backreflection can be in resonance with both beams but, due to the Doppler shift, with different resonance frequencies defined by the different atomic hyperfine levels. These atoms contribute permanently to the absorption process and therefore enhance the absorption signal drastically. This explanation is strongly supported by theoretical considerations, previous observations [17] as well as a second experiment (fig. 13.15), where two beams counter-propagating through sodium vapor (produced by an atom dispenser outside the sandwich cell) show the same behavior.

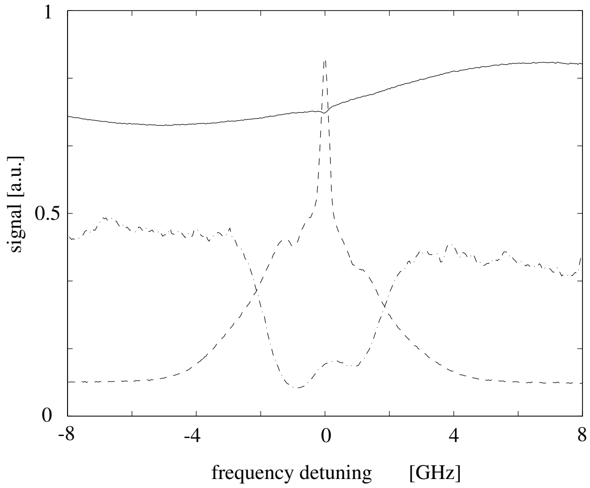

Figure 13.15: *Solid line: absorption profile of one of the two counter-propagating beams; dashed line: fluorescent spectrum perpendicular to the counter-propagating beams; dash-dotted line: transmitted power through the reference cell.*

References

[1] T. Greber, J. Wider, E. Wetli, J. Osterwalder, Phys. Rev. Lett. 81 (1998) 1654.

[2] A. Nagashima, N. Tejima, Y. Gamou, T. Kawai, C. Oshima, Phys. Rev. Lett. 75 (1995) 3918.

[3] W. Auwärter, T. J. Kreutz, T. Greber, J. Osterwalder, Surf. Sci., in press.

[4] M. Aeschlimann, E. Hull, J. Cao, C. A. Schmutternmaer, L. G. Jahn, Y. Gao, H. E. Elsayed-Ali, D. A. Mantell, and M. R. Scheinfein, Rev. Sci. Instrum. 66 (1995) 1000.

[5] J. Carpinelli, H. Weitering, E. W. Plummer, R. Stumpf, Nature 381 (1996) 498.

[6] T. Greber, J. Osterwalder, Chem. Phys. Lett. 256 (1996) 653.

[7] J. Osterwalder, T. Greber, P. Aebi, R. Fasel, L. Schlapbach, Phys. Rev. B 53 (1996) 10209.

[8] G. Held, J. Schuler, W. Sklarek, H.-P. Steinrück, Surf. Sci. 398 (1998) 154.

[9] T. Greber, T. J. Kreutz, J. Osterwalder, Phys. Rev. Lett. 79 (1997) 4465.

[10] P. Schwaller, S. Berner, T. Greber, J. Osterwalder, H. Berger, Appl. Phys. Lett., in press.

[11] G. A. Prinz, Science 282 (1999) 1660.

[12] M. D. Stiles, Phys. Rev. B 48 (1993) 7238.

[13] J. de la Figuera, J. E. Prieto, G. Kostka, S. Müller, C. Ocal, R. Miranda, K. Heinz, Surf. Sci. 349 (1996) L139.

[14] S. D. Kevan, R. H. Gaylord, Phys. Rev. B 36 (1987) 5809.

[15] S. Dangel, P. Eschle, B. Röhricht, U. Rusch, H. Schmid, and R. Holzner, J. Opt. Soc. Am. B 12 (1995) 681.

[16] R. Holzner, J. Simonet, L. Flepp, B. Röhricht, P. Eschle, S. Dangel,U. Rusch, H. Schmid, and E. Brun, Optical Engineering 34 (1995) 2315.

[17] S. Nakayama, S. Tsutsumi, Phys. Lett. 110A (1985) 368.